Configuration-based Electrical Properties Tomography

Authors: Santhosh Iyyakkunnel[1,2], Jessica Schäper[1,2] and Oliver Bieri[1,2]

Author Affiliations

[1]*Division of Radiological Physics, Department of Medical Radiology, University Hospital Basel, Basel, Switzerland*

[2]*Department of Biomedical Engineering, University of Basel, Allschwil, Switzerland*

Submitted to ***Magnetic Resonance in Medicine*** for possible publication as ***Full Paper***. ***Revision 1.***

Paper details: Abstract 238 words (max 250), Paper Body 3292 words (max 5000), 9 Figures (max 10) + 3 Supporting Information Figures, 41 References.

Key words: conductivity, electric properties, phase-cycled bSSFP, fourier transform, transceive phase, configuration space

Corresponding author:

Santhosh Iyyakkunnel

Petersgraben 4, 4031 Basel, Switzerland

E-mail: santhosh.iyyakkunnel@unibas.ch

ABSTRACT

Purpose: To introduce phase-based conductivity mapping from a configuration space analysis.

Methods: The frequency response function of balanced steady state free precession (bSSFP) is used to perform a configuration space analysis. It is shown that the transceive phase for conductivity mapping can be directly obtained by a simple Fast Fourier Transform (FFT) of a series of phase-cycled bSSFP scans. For validation, transceive phase and off-resonance mapping with FFT is compared to phase estimation using a recently proposed method, termed PLANET. Experiments were performed in phantoms and for in vivo brain imaging at 3 T using a quadrature head coil.

Results: For FFT, aliasing can lead to systematic phase errors. This bias, however, decreases rapidly with increasing sampling points. Interestingly, Monte Carlo simulations, revealed a lower uncertainty for the transceive phase and the off-resonance using FFT as compared to PLANET. Both methods, however, essentially retrieve the same phase information from a set of phase-cycled bSSFP scans. As a result, configuration-based conductivity mapping was successfully performed using eight phase-cycled bSSFP scans in the phantoms and for brain tissues. Overall, the retrieved values were in good agreement with expectations. Conductivity estimation, and mapping of the field inhomogeneities can thus be performed in conjunction with the estimation of other quantitative parameters, such as relaxation, using configuration theory.

Conclusions: Phase-based conductivity mapping can be directly estimated from a simple Fourier analysis, e.g. in conjunction with relaxometry, using a series of phase-cycled bSSFP scans.

INTRODUCTION

Electrical properties tomography (EPT) retrieves the tissues' electric permittivity (ε) and conductivity (σ) from an MRI measurement of the complex excitation field B_1^+ (1–6). In good approximation, the Maxwell equations relate the curvature in the B_1^+ magnitude and phase to the permittivity and conductivity, respectively. In practice, however, the B_1^+ magnitude and phase are not measured simultaneously but in separate scans (7–9). As a result, frequently further assumptions are made to disentangle the electric properties from each other to retrieve only the permittivity from a measurement of the B_1^+ magnitude or only the conductivity using the B_1^+ phase (3,10–15). Such EPT methods are commonly referred to as "magnitude-based" and "phase-based" EPT.

Magnitude-based EPT can make use of several existing B_1 mapping methods (16–21), and their accuracy generally defines the accuracy of the EPT results (22). In contrast, the B_1 transmit phase (φ^+) is not easily determined from an MRI experiment, since it is intertwined with the B_1 receive phase (φ^-), forming what is referred to as transceive phase ($\varphi^\pm$) (7,22). For phase-based conductivity reconstruction, however, knowledge of φ^+ is not necessarily required. Any linear combination of φ^+ and φ^- – and thus also $\varphi^\pm$ – can be used, but it is critical that estimation of the transceive phase is free from any other contribution, such as from off-resonances, and is measured with a high signal-to-noise-ratio (10,22). To this end, dedicated spin-echo methods are most common (5), but information of the transceive phase is often already contained in the measurement (22).

In fact, balanced steady state free precession (bSSFP) has recently attracted increased interest for EPT (11,23,24). Moreover, bSSFP is known for its high efficiency, delivering one of the highest signal-to-noise-ratios (SNR) per unit time (25). Off-resonances, however, are omnipresent and thus compromise a reliable transceive phase estimation. Methods to address this issue were recently proposed e.g. by Ozdemir et al. (23) using two phase-cycled bSSFP scans together with a main magnetic field inhomogeneity map (ΔB_0) and a T_2 map, or by Gavazzi et al. (11) using a least-squares fit to retrieve multiple parameters, such as T_1,T_2, ΔB_0 and also the transceive phase, from a geometrically inspired method termed PLANET.

In this work, we present an alternative approach to directly extract the transceive phase from a series of phase-cycled bSSFP scans using configuration theory, as recently suggested for relaxometry (26). It will be shown that the transceive phase and the local off-resonance are inherently linked with the configuration modes and can thus be directly retrieved using a simple Fast Fourier Transformation (FFT). Since PLANET has been thoroughly compared to conventional methods for conductivity mapping, and phase estimation is performed essentially on the same underlying set of phase-cycled bSSFP data, FFT-based conductivity mapping is validated through a direct comparison of the phase information either retrieved with PLANET or FFT in phantoms and for in vivo brain at 3 T.

METHODS

Configuration-based transceive phase estimation

For bSSFP and immediately after the RF pulse, the complex magnetization (M^+) in the steady state, as a function of the RF flip angle (α) and the tissue relaxation times T_1 and T_2, can be written in the form (e.g., cf. Ref. (27))

$$M^+(\phi) = -\frac{i}{D}(1-E_1)\sin\alpha\left(1-E_2e^{-i\phi}\right), \quad [1]$$

where

$$D \triangleq (1-E_1\cos\alpha)(1-E_2\cos\phi) + (\cos\alpha - E_1)(E_2-\cos\phi)E_2 \quad [2]$$

where $E_{1,2} \triangleq e^{-TR/T_{1,2}}$ and $\phi \triangleq \vartheta - \varphi$ denotes the phase difference between the off-resonance related phase accumulation (ϑ) during one repetition time (TR) and the RF phase increment φ. As usual, diffusion and finite RF pulse effects are neglected. Since $M^+(\phi)$ is periodic with ϕ, it can be expanded in configuration (Fourier) space, including all configuration orders $M^{(n)}$:

$$M^+(\phi) = \sum_{n=-\infty}^{\infty} e^{in\phi}M^{(n)} \quad [3]$$

At time $t = x \cdot TR$ $(0 < x < 1)$, the magnetization M, and thus the acquired signal S_ϕ, becomes

$$S_\phi(t) = \rho e^{i\varphi^\pm}M(\phi,t) = \rho e^{i\varphi^\pm}E_2^x e^{ix\vartheta}M^+(\phi) \quad [4]$$

where ρ denotes a scaling factor, $\varphi^\pm$ the transceive phase and $E_2^x \triangleq e^{-x\cdot TR/T_2}$.

As shown in a seminal work of Zur et al. (28), the configurational modes can be retrieved from sampling the bSSFP frequency response function, e.g. using a set of phase-cycled bSSFP scans

$$\left\{S_{\phi_j}(t)\middle|\phi_j \equiv \vartheta - \varphi_j : \varphi_j \triangleq -j\cdot\frac{2\pi}{N},\ j = 0,1,\dots N-1\right\} \quad [5]$$

in combination with an N-point Fourier transform

$$\begin{aligned} S^{(p)}(t) &= \frac{1}{N}\sum_{j=0}^{N-1} S_{\phi_j}(t)\, e^{-i(\frac{2\pi}{N})jp} \\ &= \rho e^{i\varphi^\pm}E_2^x e^{ix\vartheta}\frac{1}{N}\sum_{j=0}^{N-1}\sum_{n=-\infty}^{\infty} e^{in\vartheta}M^{(n)}e^{i\left(\frac{2\pi}{N}\right)j(n-p)} \end{aligned} \quad [6]$$

which yields

$$S^{(p)}(t) = \rho e^{i\varphi^{\pm}} E_2^x e^{ix\vartheta}\left(e^{ip\vartheta} M^{(p)} + e^{i(p\pm N)\vartheta} M^{(p\pm N)} + e^{i(p\pm 2N)\vartheta} M^{(p\pm 2N)} \ldots\right) \qquad [7]$$

since

$$\sum_{n=-\infty}^{\infty} e^{i\left(\frac{2\pi}{N}\right)j(n-p)} = \begin{cases} N, & if\ \dfrac{n-p}{N} \in \mathbb{Z} \\ 0, & otherwise \end{cases} \qquad [8]$$

In the steady state, the modes $M^{(p)}$ decrease exponentially with increasing configuration order $|p|$ with a decay rate that depends on the flip angle α and the relaxation time ratio T_2/T_1 (27). As a result, aliasing can be neglected in Eq. [7] for large enough N, which yields for the two lowest order components

$$S^{(0)} \approx e^{i\varphi^{\pm}} e^{ix\vartheta} M^{(0)}, \qquad S^{(-1)} \approx e^{i\varphi^{\pm}} e^{i(x-1)\vartheta} M^{(-1)} \qquad [9]$$

As a result, the off-resonance related precession angle ϑ can be directly retrieved from the argument of the configurational ratio

$$\arg\left[\frac{S^{(0)}}{S^{(-1)}}\right] = \vartheta + \arg\left[\frac{M^{(0)}}{M^{(-1)}}\right] = \vartheta - \pi \qquad [10]$$

considering that positive modes ($p \geq 0$) have a phase of $-\pi/2$, whereas negative ones ($p < 0$) have a phase of $\pi/2$ (27). Similarly, the transceive phase is obtained by the argument of the configurational product

$$\arg\left[S^{(0)} \cdot S^{(-1)}\right] = 2\varphi^{\pm} + \vartheta\left(x - \frac{1}{2}\right) + \arg\left[M^{(0)} \cdot M^{(-1)}\right] = 2\varphi^{\pm} + \vartheta\left(x - \frac{1}{2}\right) \qquad [11]$$

which becomes independent of ϑ for a centered echo ($x = 1/2$),

$$\arg\left[S^{(0)} \cdot S^{(-1)}\right] = 2\varphi^{\pm} \qquad [12]$$

Numerical simulations

In order to benchmark FFT against PLANET for transceive phase mapping, bSSFP signal simulations were performed using a TR (TE) of 4.6 (2.3) ms, a flip angle of 25° and a T_1/T_2 = 832 ms / 80 ms, as suggested for PLANET by Gavazzi et al. (11). According to Eq. [5], signals were simulated for N = 8 and N = 16 phase-cycling steps. The simulated complex bSSFP signals were then subjected to a N-point Fourier transform yielding the configurational modes $S^{(p)}$ (reaching from $p = -N/2$ to $p = N/2 - 1$). The results were then compared to the limit of continuous RF phase increments to assess possible systematic errors in the transceive phase and off-resonance due to discrete sampling.

In addition, Monte Carlo simulations were performed to assess random noise propagation in both, FFT and PLANET, as a function of the flip angle and TR using 10000 drawings. To this end, Gaussian noise

with a standard deviation of 1/1000 M_0 (with $M_0 = 1$) was added independently to the real and imaginary part of the simulated bSSFP signals. TR was varied from 1 ms to 33 ms while the flip angle covered the range from 0° to 90°. Furthermore, as in Gavazzi et al. (11), the off-resonance was set to 15 Hz and the transceive phase to −60°.

All simulations and calculations were performed in MatLab (R2019a, MathWorks, Natick, MA).

Imaging experiments

Imaging was performed at 3 T (Magnetom Prisma, Siemens Healthcare, Erlangen, Germany) using a dual tuned 1H/23Na quadrature head coil for transmission and reception (Rapid Biomedical GmbH, Rimpar, Germany). For the phantom scans, two bottles with 2 g/L and 8.8 g/L sodium chloride were prepared, yielding an estimated electrical conductivity of 0.34 S/m and 1.39 S/m, respectively (29). In addition, the saline solutions had 0.125 mM MnCl to provide tissue comparable relaxation times (T1 ~ 870 ms, T2 ~ 70 ms).

For configuration-based analysis, eight phase-cycled 3D bSSFP scans were acquired with RF phase increments of 0°, 45°, 90°, 135°, 180°, 225°, 270°, 315°. Slab-selective excitation with a flip angle of 25° was used. For the phantom scans, a TR (TE) of 4.6 ms (2.3 ms) was used and the voxel size was set to 1.3x1.3x1.3 mm^3 for an imaging matrix of 192x168x120 with 20 % slice oversampling, elliptical scanning and 343 Hz/px bandwidth. A single bSSFP scan took 92 s and scanning was completed in about 12 min. For the in vivo scans, a TR (TE) of 3.13 ms (1.57 ms) was used. As for the phantom scan, the same imaging matrix of 192x168x120 with 20 % slice oversampling and elliptical scanning was used, yielding a voxel size of 1.3x1.3x1.3 mm^3, interpolated to 0.7 mm isotropic (using the scanner software provided by the manufacturer). The bandwidth was set to 790 Hz/px. A single bSSFP scan took 76 s and overall scanning was completed in less than 10 min. To ensure proper steady state conditions, 1000 dummy TRs were used.

In vivo scans were approved by the local Ethics Board.

Transceive phase estimation and conductivity mapping

First, to account for possible movements between the phase-cycled scans, the in vivo brain scans were rigidly registered using elastix (30) prior to any postprocessing. Then, the complex modes, entering Eqs. [10] and [12], are retrieved from the sampled complex bSSFP frequency response function using FFT. In contrast, PLANET makes use of the same phase-cycled bSSFP data but analyses the signal geometrically in the complex plane. As the magnitude of the complex phase-cycled signal of a voxel follows the bSSFP frequency response, the signal forms an ellipse in the complex plane. The ellipse

holds information about the voxel's properties such as T_1, T_2, ΔB_0 and $\varphi^{\pm}$. PLANET was implemented as described by Shcherbakova et al. (31) and Gavazzi et al. (11) using a numerically stable direct least squares ellipse fit (32–34). The off-resonance and transceive phase maps were unwrapped using an in-house developed phase unwrapping algorithm.

Subsequently, the local conductivity was reconstructed from the transmit phase φ^{+} via the simplified homogenous Helmholtz equation (35) using the transceive phase assumption, $\varphi^{+} = \varphi^{\pm}/2$:

$$\sigma \approx \frac{\nabla^2 \varphi^{\pm}}{2\mu_0 \omega} \qquad [13]$$

This approximation of the transmit phase holds for field strengths up to 3 T when a quadrature birdcage coil is used for excitation and reception and when the scanned object is of cylindrical form (7). In Eq. [13], μ_0 is the magnetic vacuum permeability and ω is the Larmor frequency.

The Laplacian was estimated using the coefficients of a locally fitted second-order polynomial, restricted to voxels with magnitude values similar to the center point of the window (36). The Laplace estimate was subsequently smoothed with a tissue boundary preserving median filter and a 2D Gaussian bilateral filter (using imbilatfilt from Matlab with the degree of smoothing set to 0.1) (10,36). The window size for both the Laplace estimation and the median filter was set to 9×9×9 px^3 for the phantom scans and 21×21×21 px^3 for the interpolated in-vivo scans.

The uncertainty in the phase image ($SD_{\varphi^{\pm}}$) in radians can be generally estimated by the inverse of the signal-to-noise-ratio (SNR) of the magnitude image SNR_{Magn} (37,38):

$$SD_{\varphi^{\pm}} = \left(SNR_{Magn}\right)^{-1} \qquad [14]$$

In this work, the transceive phase $\varphi^{\pm}$ results from the product of two configurational mode images (cf. Eq. [12]). The SNR_{Magn} is thus related to the SNR of the individual mode images, according to

$$SNR_{Magn} = \left[\left(SNR_{Magn}^{S^{(0)}}\right)^{-2} + \left(SNR_{Magn}^{S^{(-1)}}\right)^{-2}\right]^{-1} \qquad [15]$$

A detailed derivation of this relation is given in Appendix A.

RESULTS

The complex signal of bSSFP (cf. Eq. [4]) is shown in Figure 1A for tissues and for a centered echo in magnetization and configuration space. For eight phase-cycled scans, the retrieved configurational modes using FFT coincide almost perfectly with the ideal result, that is for a continuous RF phase

increment. Generally, however, aliasing can lead to deviations which become more conspicuous for higher order modes. This can lead to a systematic error for the FFT-based estimation of ΔB_0 and $\varphi^{\pm}$, as shown in Figure 1B for 8 and 16 phase-cycling steps, but decreases rapidly with increasing number of RF phase increments (26). Overall, from the discrete sampling, the error, as a function of the off-resonance related phase accumulation, undergoes a harmonic modulation with a period of $2\pi/N$.

Generally, it can also be expected that the FFT-based systematic error in the estimation of ΔB_0 and $\varphi^{\pm}$ depends on the shape of the frequency response function and thus on T_2/T_1 (in the limit of $TR << T_2$) and on the flip angle. Figure 2 shows the maximum systematic error for both ΔB_0 and $\varphi^{\pm}$ as a function of relaxation times for a fixed flip angle (α = 25°). Notably, the maximum systematic error for $\varphi^{\pm}$ estimation is approximately one order of magnitude lower than for ΔB_0 (see also Figure 1B).

Noise leading to random phase accruals in the estimation of ΔB_0 and $\varphi^{\pm}$ is evaluated and compared in Figure 3 for both methods, FFT and PLANET, as a function of the TR and flip angle. For tissues, the recommended settings for PLANET (TR = 4.6 ms and flip angle α = 25°) yield a transceive phase uncertainty that is approximately 30 % higher than the one using FFT, whereas for the local off-resonance, the error is more than 3 times less using FFT as compared to PLANET.

For the phantom scan, off-resonance maps and transceive phase images estimated with both methods, FFT and PLANET, are shown for comparison in Figures 4 and 5. The corresponding set of phase-cycled magnitude and phase images, as well as their pendant in Fourier space, are shown in Supporting Information Figures S1 and S2. Apart from minor phase unwrapping errors at the edges, ΔB_0 (Figure 4A) and $\varphi^{\pm}$ (Figure 5A) appear visually identical for both methods. This finding is confirmed by line plots for ΔB_0 (Figure 4B) and $\varphi^{\pm}$ (Figure 5B). As a result, except for the expected different noise behavior, both methods essentially retrieve the same phase information from the underlying set of phase-cycled bSSFP data. For the FFT, the SNR_{Magn} (cf. Eq. [15]) of the phantom scan is found to be around 300, yielding a transceive phase uncertainty of $SD_{\varphi^{\pm}}$ = 1/300 rad.

The product of the magnitude images of the two lowest configurational modes, together with a reconstruction of the conductivity using Eq. [13], is shown in Figure 6. The results without the application of the boundary-preserving median filter are shown in Supporting Information Figure S3A. For the phantom with the lower salt concentration, a bulk conductivity of 0.43 ± 0.04 S/m was measured. For the high saline phantom, a conductivity of 1.46 ± 0.08 S/m was observed.

In complete analogy, complex configuration modes are derived using Fourier transformation of the set of eight phase-cycled in-vivo bSSFP brain scans (data not shown). Resulting axial phase images for the off-resonance and the transceive phase using FFT and PLANET are shown in Figures 7 and 8. The retrieved phase information is essentially identical for both methods. In contrast to the phantom results, however, the different noise performance of FFT and PLANET becomes visually noticeable especially

in the retrieved ΔB_0 maps (Figure 7). In contrast, transceive phase images for FFT and PLANET show a similar noise level (Figure 8A), as confirmed by the line profiles (Figure 8B). In this case, as the SNR_{Magn} (cf. Eq. [15]) averaged over the whole brain was found to be around 100, resulting in a transceive phase uncertainty of $SD_{\varphi^{\pm}}$ = 1/100 rad.

Finally, Figure 9 shows a collection of axial corresponding magnitude and conductivity brain images (corresponding results before the application of the median filter are shown in Supporting Information Figure S3B). For selected regions-of-interest (ROI) in different tissues of the brain conductivity values were retrieved. For white matter (ROI 1) a value of 0.44 ± 0.01 S/m was observed. Cortical gray matter (ROI 2) showed a conductivty of 0.73 ± 0.01 S/m. For the putamen (ROI 3) a conductivity of 0.61 ± 0.01 S/m was obtained. A conductivity of 0.77 ± 0.02 S/m was measured for the thalamus (ROI 4) while cerebrospinal fluid (ROI 5) yielded the highest conductivity value of 1.89 ± 0.08 S/m.

DISCUSSION

Under ideal conditions, such as at on-resonance or in the limit of TR << T_2 for low off-resonance related precession, bSSFP is able to provide an estimate of the transceive phase. Generally, even for the brain, off-resonances can become quite severe and in turn the TR not sufficiently short that these criteria can be fulfilled throughout. As a result, multiple phase-cycled bSSFP scans need to be acquired. In this work, we have shown that configuration theory provides direct access to the transceive phase from such a set of phase-cycled bSSFP scans. Similary, configuration theory was recently suggested for relaxometry (26,39). Thus, essentially the same framework can be used to gain access not only to tissue relaxometry but also to conductivity mapping.

Recently, a different framework, termed PLANET, was proposed to extract relaxation parameters, as well as the local off-resonance and the transceive phase information, from a set of phase-cycled bSSFP scans (11,31). Notably, Gavazzi et al. (11) performed a thorough validation of PLANET for phase-based EPT. Thus, for validation purposes, we compared FFT to PLANET, since both methods can be run on essentially the same data sets. To this end, imaging and simulations were performed with the recommended settings for PLANET (11).

Generally, estimation of the configurational states from a finite number of samples using FFT is prone to aliasing (28), as reflected by a residual oscillitaing systematic bias, but can easily be mitigated by using a higher number of phase-cycles (cf. Figure 1B). Interestingly, Monte Carlo simulations revealed that there is lower noise propagation in FFT not only for typical bSSFP settings, that is TR < 10 ms and flip angle $\alpha > 10°$, but generally over almost the whole range of simulated values for the repetition time and flip angle compared to PLANET (cf. Figure 3). This finding might be due to the model-based

complex least-squares estimator used for PLANET whereas FFT only relies on a periodicity assumption of the signal which might be less sensitive to outliers.

As with tissue relaxometry, conductivity can be biased by many factors. Besides the fact that tissues are not pure, conductivity mapping also relies on an estimation of the not directly accessible transmit phase using the transceive phase assumption. Generally, the validity of this assumption reduces for non-cylindrical geometries, such as the head, or with increasing Larmor frequency (7).

The retrieved conductivity values in the phantoms are close to the expectations but appear to overestimate the underlying conductivity values. This might be either due to a bias between the real and estimated conductivity based on the salt concentrations or due the used conductivity reconstruction based on Eq. [13]. It is known that the simplified homogenous Helmholtz equation for phase-based EPT yields higher conductivity values as expected due to neglected gradient terms of the complex B_1^+-field (7,22,35). It is assumed that with reconstruction algorithms based on the full Helmholtz equation more accurate results can be achieved (8,9,13). Especially for tissue, other factors might lead to deviations, such as asymmetries in the bSSFP's frequency response profile (40,41). But in general, brain tissue conductivities are in good agreement with what is reported in the literature for phase-based EPT (7,35).

In complete analogy to the recently proposed PLANET methodology (11,31), configuration-based transceive phase estimation builds up on a set of phase-cycled bSSFP scans. In this work, the transceive phase separates from the estimation of tissue relaxivities and becomes directly accessible by means of a simple Fourier transform, whereas PLANET requires least-square fitting of a bSSFP signal model. Generally, as with PLANET, conductivity mapping can be performed in conjunction with tissue relaxometry, and thus without the need of additional scans or scan time.

CONCLUSION

In conclusion, we have shown that the transmit phase and thus the conductivity can be directly estimated from a set of phase-cycled bSSFP scans using straightforward arithemtics. The validity of the proposed methodology was confirmed in phantoms and the feasibility was demonstrated for brain in vivo. From a set of phase-cycled bSSFP scans, conductivity mapping can be performed in conjunction with tissue relaxation, and thus without scan time prolongation. Overall, this might facilitate successful translation of conductivity mapping into the clinical setting.

ACKNOWLEDGEMENTS

This work was supported by the Swiss National Science Foundation (SNF grant No. 325230_182008). We thank Carl Ganter for helpful discussions.

APPENDIX A

For the derivation of the magnitude SNR of the product of two images we consider two signals

$$s_{1,2} = x_{1,2} + n_{1,2} \qquad \text{[A1]}$$

with constant amplitude (x) and Gaussian noise (n) of variance

$$\sigma_{1,2}^2 = \langle \left(s_{1,2} - x_{1,2}\right)^2 \rangle = \langle {n_{1,2}}^2 \rangle \qquad \text{[A2]}$$

and mean

$$\langle s_{1,2} \rangle = x_{1,2}, \qquad \langle n_{1,2} \rangle = 0, \qquad \langle n_1 n_2 \rangle = 0 \qquad \text{[A3]}$$

For the product s of the two signals,

$$s = s_1 \cdot s_2 = x_1 x_2 + x_1 n_2 + x_2 n_1 + n_1 n_2 \equiv x + n \qquad \text{[A4]}$$

with

$$x \triangleq x_1 x_2, \qquad n \triangleq x_1 n_2 + x_2 n_1 + n_1 n_2, \qquad \text{[A5]}$$

we find the variance

$$\begin{aligned} \sigma^2 = \langle (s - x_1 x_2)^2 \rangle = \langle (x_1 n_2 + x_2 n_1 + n_1 n_2)^2 \rangle = \cdots \\ = \mathrm{x}_1^2 \sigma_2^2 + \mathrm{x}_2^2 \sigma_1^2 + O(n^4) \end{aligned} \qquad \text{[A6]}$$

Assuming a reasonable SNR, that is $\langle x_{1,2} \rangle \gg \sigma_{1,2}$, we thus find

$$|SNR|^{-2} \triangleq \frac{\sigma^2}{\mathrm{x}^2} \approx \frac{\mathrm{x}_1^2 \sigma_2^2 + \mathrm{x}_2^2 \sigma_1^2}{x_1^2 x_2^2} = |SNR_2|^{-2} + |SNR_1|^{-2} \qquad \text{[A7]}$$

For the magnitude SNR of the individual mode images ($SNR_{1,2}$), the ratio was taken between the average signal magnitude within the object and the standard deviation of the real part of the image in the background (air).

REFERENCES

1. Haacke EM, Petropoulos LS, Nilges EW, Wu DH. Extraction of conductivity and permittivity using magnetic resonance imaging. Phys. Med. Biol. 1991;36:723–734 doi: 10.1088/0031-9155/36/6/002.

2. Wen H. Noninvasive quantitative mapping of conductivity and dielectric distributions using RF wave propagation effects in high-field MRI. In: Medical Imaging 2003: Physics of Medical Imaging. Vol. 5030. International Society for Optics and Photonics; 2003. pp. 471–477. doi: 10.1117/12.480000.

3. Katscher U, Voigt T, Findeklee C, Vernickel P, Nehrke K, DÖssel O. Determination of Electric Conductivity and Local SAR Via B1 Mapping. IEEE Trans. Med. Imaging 2009;28:1365–1374 doi: 10.1109/TMI.2009.2015757.

4. Liu J, Wang Y, Katscher U, He B. Electrical Properties Tomography Based on B1 Maps in MRI: Principles, Applications, and Challenges. IEEE Trans. Biomed. Eng. 2017;64:2515–2530 doi: 10.1109/TBME.2017.2725140.

5. Katscher U, Berg CAT van den. Electric properties tomography: Biochemical, physical and technical background, evaluation and clinical applications. NMR Biomed. 2017;30:e3729 doi: 10.1002/nbm.3729.

6. Zhang X, Liu J, He B. Magnetic Resonance Based Electrical Properties Tomography: A Review. IEEE Rev. Biomed. Eng. 2014;7:87–96 doi: 10.1109/RBME.2013.2297206.

7. Lier ALHMW van, Raaijmakers A, Voigt T, et al. Electrical Properties Tomography in the Human Brain at 1.5, 3, and 7T: A Comparison Study. Magn. Reson. Med. 2014;71:354–363 doi: 10.1002/mrm.24637.

8. Liu J, Zhang X, Schmitter S, Moortele P-FV de, He B. Gradient-based electrical properties tomography (gEPT): A robust method for mapping electrical properties of biological tissues in vivo using magnetic resonance imaging. Magn. Reson. Med. 2015;74:634–646 doi: 10.1002/mrm.25434.

9. Hafalir FS, Oran OF, Gurler N, Ider YZ. Convection-Reaction Equation Based Magnetic Resonance Electrical Properties Tomography (cr-MREPT). IEEE Trans. Med. Imaging 2014;33:777–793 doi: 10.1109/TMI.2013.2296715.

10. Lee J, Shin J, Kim D-H. MR-based conductivity imaging using multiple receiver coils. Magn. Reson. Med. 2016;76:530–539 doi: 10.1002/mrm.25891.

11. Gavazzi S, Shcherbakova Y, Bartels LW, et al. Transceive phase mapping using the PLANET method and its application for conductivity mapping in the brain. Magn. Reson. Med. 2020;83:590–607 doi: 10.1002/mrm.27958.

12. Hampe N, Herrmann M, Amthor T, Findeklee C, Doneva M, Katscher U. Dictionary-based electric properties tomography. Magn. Reson. Med. 2019;81:342–349 doi: 10.1002/mrm.27401.

13. Gurler N, Ider YZ. Gradient-based electrical conductivity imaging using MR phase. Magn. Reson. Med. 2017;77:137–150 doi: 10.1002/mrm.26097.

14. Katscher U, Börnert P. Imaging of Lung Conductivity Using Ultrashort Echo-Time Imaging. In: Singapore, Singapore; 2015. p. Abstract no. 2923.

15. Lier ALHMW van, Brunner DO, Pruessmann KP, et al. B1+ Phase mapping at 7 T and its application for in vivo electrical conductivity mapping. Magn. Reson. Med. 2012;67:552–561 doi: 10.1002/mrm.22995.

16. Ganter C, Settles M, Dregely I, Santini F, Scheffler K, Bieri O. B1-mapping with the transient phase of unbalanced steady-state free precession. Magn. Reson. Med. 2013;70:1515–1523 doi: 10.1002/mrm.24598.

17. Nehrke K, Börnert P. DREAM—a novel approach for robust, ultrafast, multislice B1 mapping. Magn. Reson. Med. 2012;68:1517–1526 doi: 10.1002/mrm.24158.

18. Sacolick LI, Wiesinger F, Hancu I, Vogel MW. B1 mapping by Bloch-Siegert shift. Magn. Reson. Med. 2010;63:1315–1322 doi: 10.1002/mrm.22357.

19. Stollberger R, Wach P. Imaging of the active B1 field in vivo. Magn. Reson. Med. 1996;35:246–251 doi: 10.1002/mrm.1910350217.

20. Yarnykh VL. Actual flip-angle imaging in the pulsed steady state: A method for rapid three-dimensional mapping of the transmitted radiofrequency field. Magn. Reson. Med. 2007;57:192–200 doi: 10.1002/mrm.21120.

21. Gavazzi S, Berg CAT van den, Sbrizzi A, et al. Accuracy and precision of electrical permittivity mapping at 3T: the impact of three mapping techniques. Magn. Reson. Med. 2019;81:3628–3642 doi: 10.1002/mrm.27675.

22. Katscher U, Kim D-H, Seo JK. Recent Progress and Future Challenges in MR Electric Properties Tomography. Comput. Math. Methods Med. 2013;2013 doi: 10.1155/2013/546562.

23. Ozdemir S, Ider YZ. bSSFP phase correction and its use in magnetic resonance electrical properties tomography. Magn. Reson. Med. 2019;81:934–946 doi: 10.1002/mrm.27446.

24. Stehning C, Voigt T, Katscher U. Real-Time Conductivity Mapping using Balanced SSFP and Phase-Based Reconstruction. In: Vol. 19. Montreal, Canada; 2010. p. 128.

25. Bieri O, Scheffler K. Fundamentals of balanced steady state free precession MRI. J. Magn. Reson. Imaging JMRI 2013;38:2–11 doi: 10.1002/jmri.24163.

26. Nguyen D, Bieri O. Motion-insensitive rapid configuration relaxometry. Magn. Reson. Med. 2017;78:518–526 doi: 10.1002/mrm.26384.

27. Ganter C. Static susceptibility effects in balanced SSFP sequences. Magn. Reson. Med. 2006;56:687–691 doi: 10.1002/mrm.20986.

28. Zur Y, Wood ML, Neuringer LJ. Motion-insensitive, steady-state free precession imaging. Magn. Reson. Med. 1990;16:444–459 doi: 10.1002/mrm.1910160311.

29. Stogryn A. Equations for Calculating the Dielectric Constant of Saline Water (Correspondence). IEEE Trans. Microw. Theory Tech. 1971;19:733–736 doi: 10.1109/TMTT.1971.1127617.

30. Klein S, Staring M, Murphy K, Viergever MA, Pluim JPW. elastix: A Toolbox for Intensity-Based Medical Image Registration. IEEE Trans. Med. Imaging 2010;29:196–205 doi: 10.1109/TMI.2009.2035616.

31. Shcherbakova Y, Berg CAT van den, Moonen CTW, Bartels LW. PLANET: An ellipse fitting approach for simultaneous T1 and T2 mapping using phase-cycled balanced steady-state free precession. Magn. Reson. Med. 2018;79:711–722 doi: 10.1002/mrm.26717.

32. Chernov N. Ellipse Fit (Direct method). MathWorks File Exchange Web Site. https://www.mathworks.com/matlabcentral/fileexchange/22684-ellipse-fit-direct-method. Published 2020. Accessed June 15, 2020.

33. Fitzgibbon A, Pilu M, Fisher RB. Direct least square fitting of ellipses. IEEE Trans. Pattern Anal. Mach. Intell. 1999;21:476–480 doi: 10.1109/34.765658.

34. Halır R, Flusser J. Numerically Stable Direct Least Squares Fitting Of Ellipses. Proc 6th Int Conf Cent Eur Comput Graph Vis 1998;98:125–132.

35. Voigt T, Katscher U, Doessel O. Quantitative conductivity and permittivity imaging of the human brain using electric properties tomography. Magn. Reson. Med. 2011;66:456–466 doi: 10.1002/mrm.22832.

36. Katscher U, Djamshidi K, Voigt T, et al. Estimation of Breast Tumor Conductivity using Parabolic Phase Fitting. In: Melbourne, Australia; 2012. p. Abstract no. 3482.

37. Gudbjartsson H, Patz S. The rician distribution of noisy mri data. Magn. Reson. Med. 1995;34:910–914 doi: 10.1002/mrm.1910340618.

38. Conturo TE, Smith GD. Signal-to-noise in phase angle reconstruction: Dynamic range extension using phase reference offsets. Magn. Reson. Med. 1990;15:420–437 doi: 10.1002/mrm.1910150308.

39. Heule R, Ganter C, Bieri O. Triple echo steady-state (TESS) relaxometry. Magn. Reson. Med. 2014;71:230–237 doi: 10.1002/mrm.24659.

40. Miller KL. Asymmetries of the balanced SSFP profile. Part I: Theory and observation. Magn. Reson. Med. 2010;63:385–395 doi: 10.1002/mrm.22212.

41. Miller KL, Smith SM, Jezzard P. Asymmetries of the balanced SSFP profile. Part II: White matter. Magn. Reson. Med. 2010;63:396–406 doi: 10.1002/mrm.22249.

FIGURES

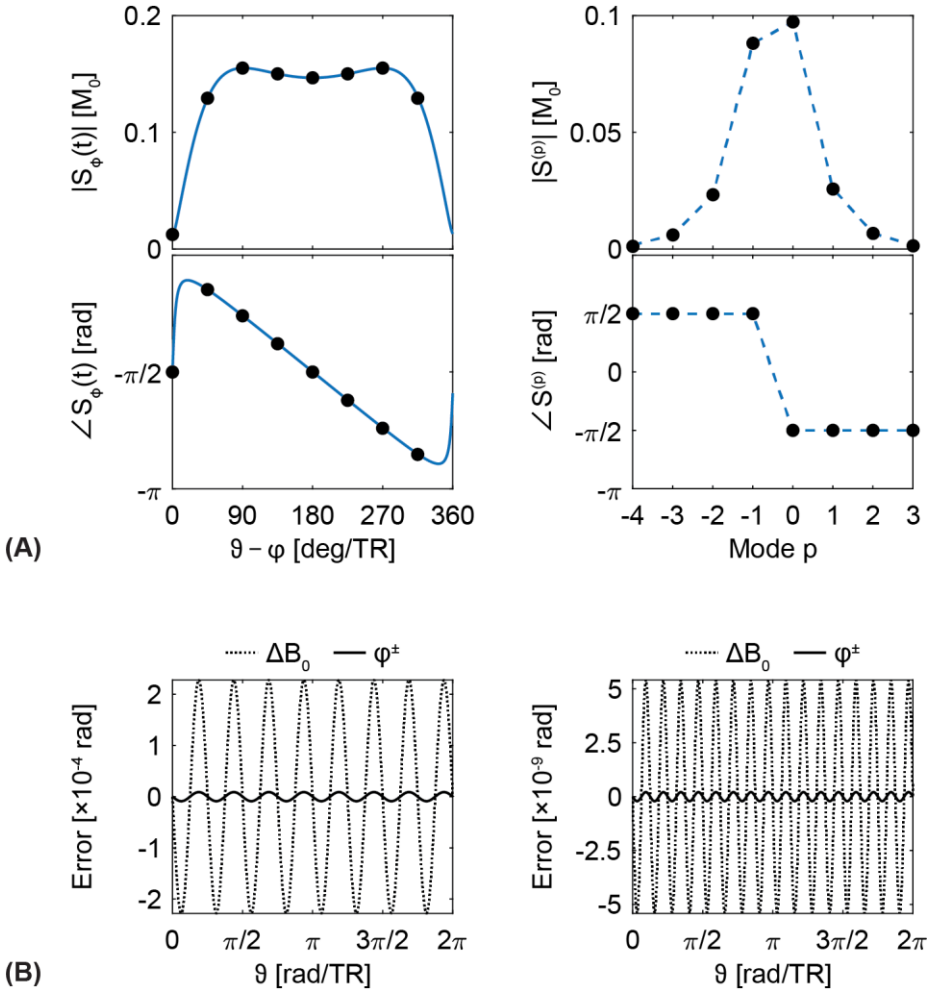

Figure 1. (A) On-resonance steady state bSSFP signal S_ϕ (left) and corresponding modes $S^{(p)}$ (right) for N = 8 phase cycles (black dots) and for a continuous RF phase increment (blue line). The dashed blue line connecting the discrete configurational modes only serves visual purpose and has no physical meaning. (B) The systematic error of ΔB_0 and $\varphi^{\pm}$ estimation as a function of the off-resonance for N = 8 (left) and N = 16 (right) phase-cycling steps. (The simulation was performed for a tissue with $\rho = 1$, a T_1 / T_2 = 832 ms / 80 ms, a TR (TE) = 4.6 (2.3) ms, a flip angle α = 25°, and for $\varphi^{\pm} = 0$; M_0 is the equilibrium magnetization).

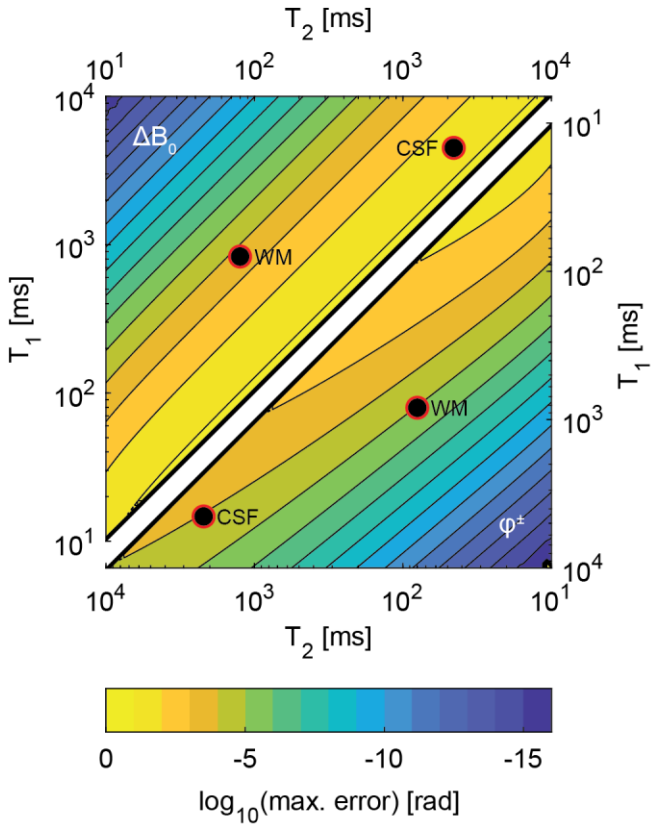

Figure 2. Maximum systematic error (see Figure 1B) as a function of T_1 and T_2. Locations of WM (T_1 / T_2 = 832 ms / 80 ms) and CSF (T_1 / T_2 = 4500 ms / 2200 ms) are indicated in the plot. (Other simulation parameters were identical to Figure 1).

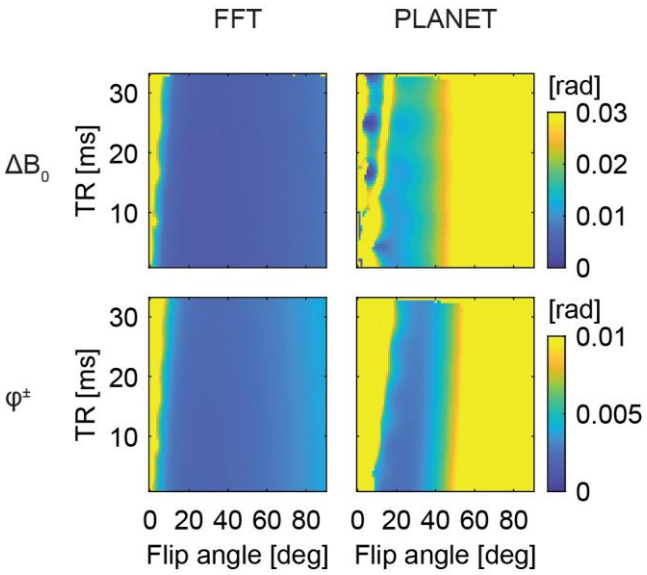

Figure 3. The uncertainty of ΔB_0 and $\varphi^{\pm}$ with respect to TR and flip angle using FFT and PLANET (Simulation parameters were: T_1 / T_2 = 832 ms / 80 ms, $\vartheta = 15$ Hz, $\varphi^{\pm} = -60°$, TR = {1, 1.5, 2, ... 32.5, 33} ms and flip angle = {0, 1, ..., 90}°, and TE = TR/2).

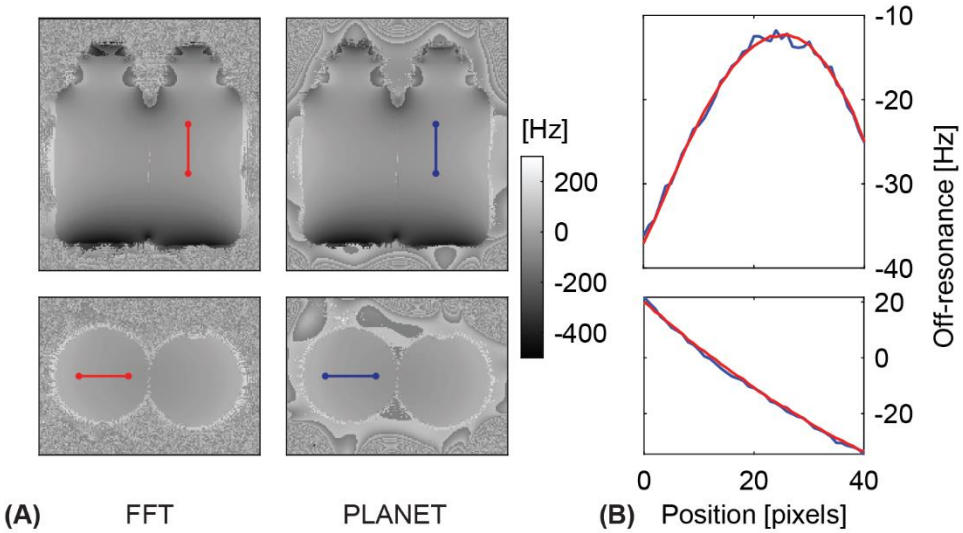

Figure 4. (A) Exemplary coronal and axial ΔB_0 maps for the phantom scan calculated using FFT and PLANET. (B) Line profiles for the two post processing methods. The locations are indicated by the colored lines in (A).

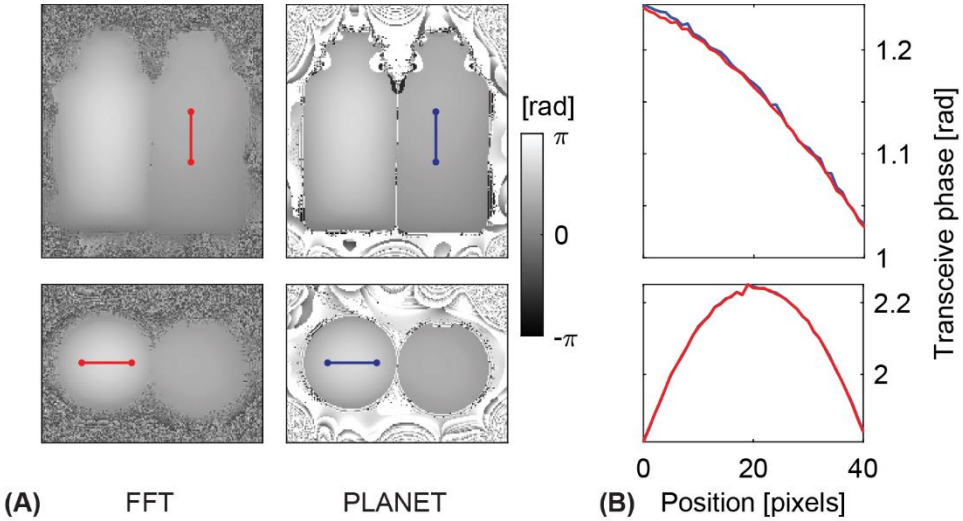

Figure 5. (A) Exemplary coronal and axial transceive phase $\varphi^{\pm}$ maps for the phantom scan calculated using FFT and PLANET. (B) Line profiles for the two post processing methods. The locations are indicated by the colored lines in (A).

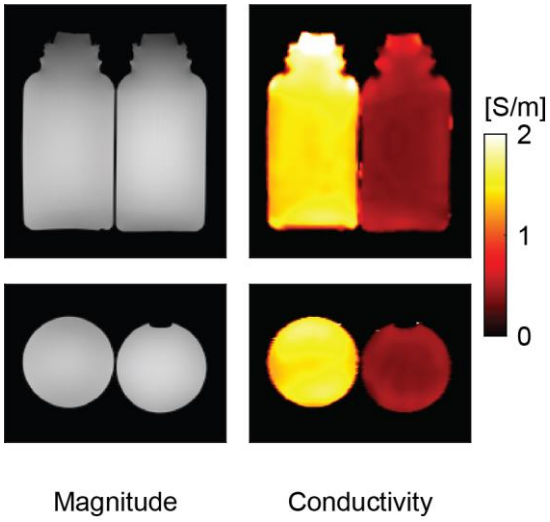

Figure 6. Exemplary coronal and axial image of the reconstructed band-free magnitude and conductivity (cf. Eq. [13]) of the phantoms. For the conductivity in the bulk, values of 1.46 ± 0.08 S/m (left) and 0.42 ± 0.04 S/m (right) are found.

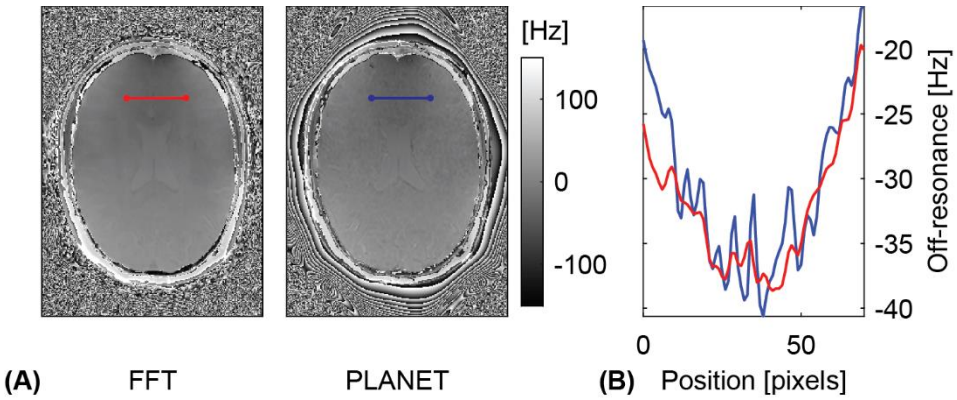

Figure 7. (A) Exemplary axial ΔB_0 maps for the in-vivo brain scan calculated using FFT and PLANET. (B) Line profiles for the two post processing methods. The locations are indicated by the colored lines in (A).

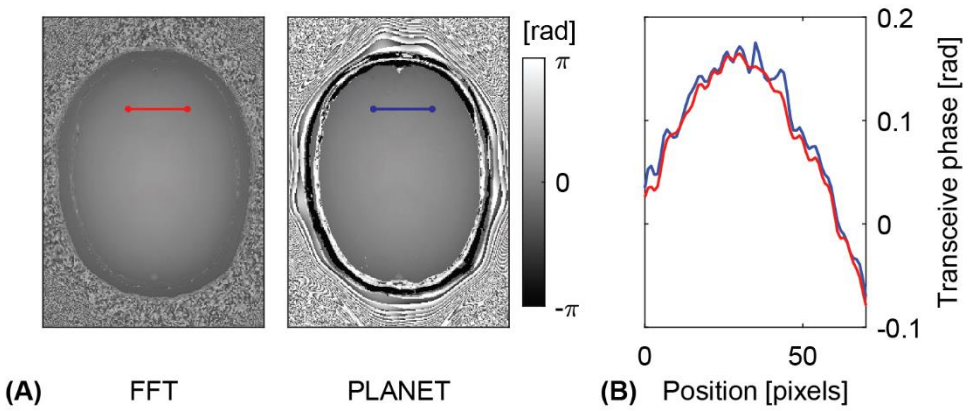

Figure 8. (A) Exemplary axial transceive phase $\varphi^{\pm}$ maps for the in-vivo brain scan calculated using FFT and PLANET. (B) Line profiles for the two post processing methods. The locations are indicated by the colored lines in (A).

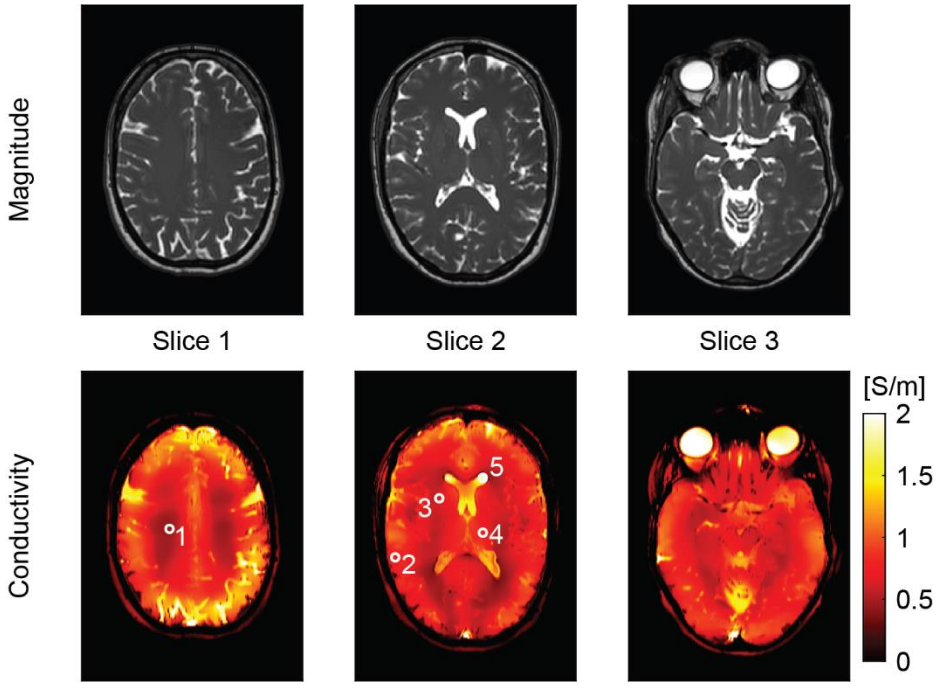

Figure 9. Exemplary axial slices of the reconstructed band-free magnitude (top row) and conductivity (bottom row) for the brain of a volunteer. The ROIs indicate locations where a value for the conductivity was retrieved for different brain tissues, with ROI 1 indicating white matter, ROI 2 cortical gray matter, ROI 3 putamen, ROI 4 thalamus and ROI 5 cerebrospinal fluid.

Configuration-based Electrical Properties Tomography

Supporting Information

Santhosh Iyyakkunnel[1,2], Jessica Schäper[1,2] and Oliver Bieri[1,2]

[1]*Division of Radiological Physics, Department of Medical Radiology, University Hospital Basel, Basel, Switzerland*

[2]*Department of Biomedical Engineering, University of Basel, Allschwil, Switzerland*

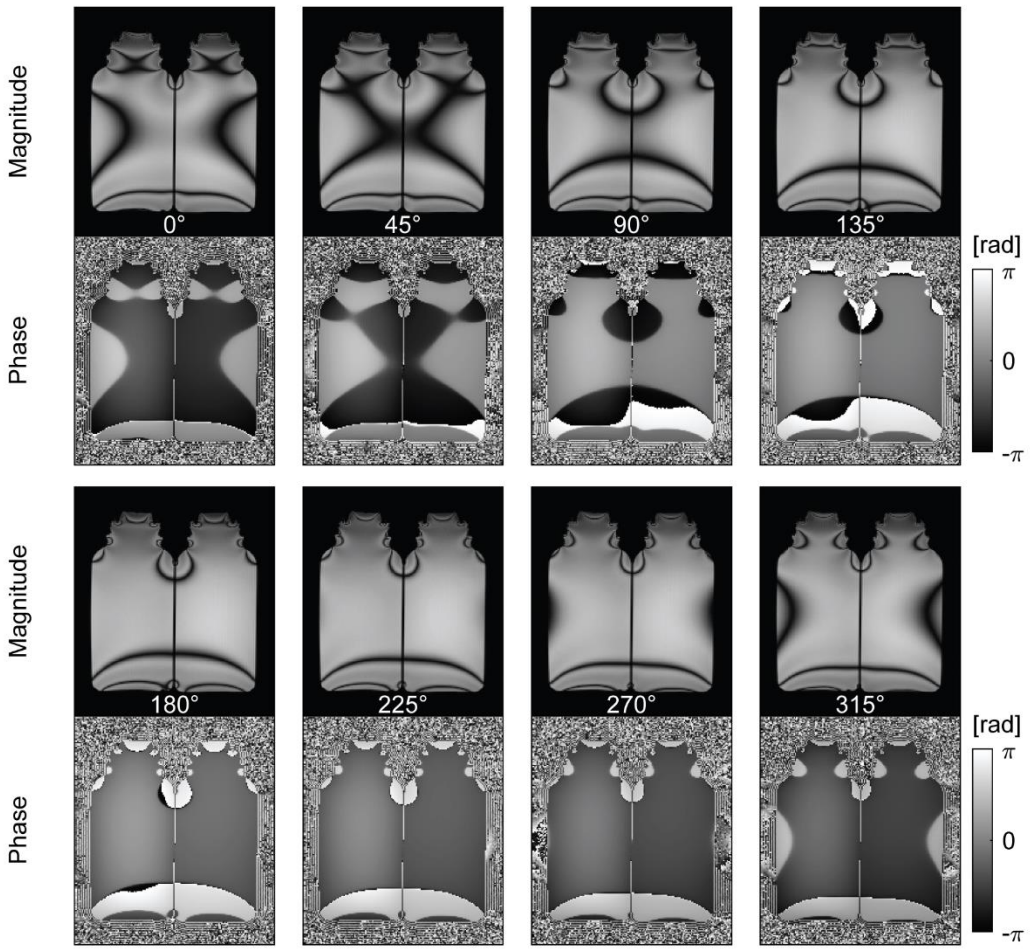

Supporting Information Figure S1 Exemplary magnitude and phase images of the phantoms from the set of eight phase-cycled bSSFP volume scans with different RF phase increment.

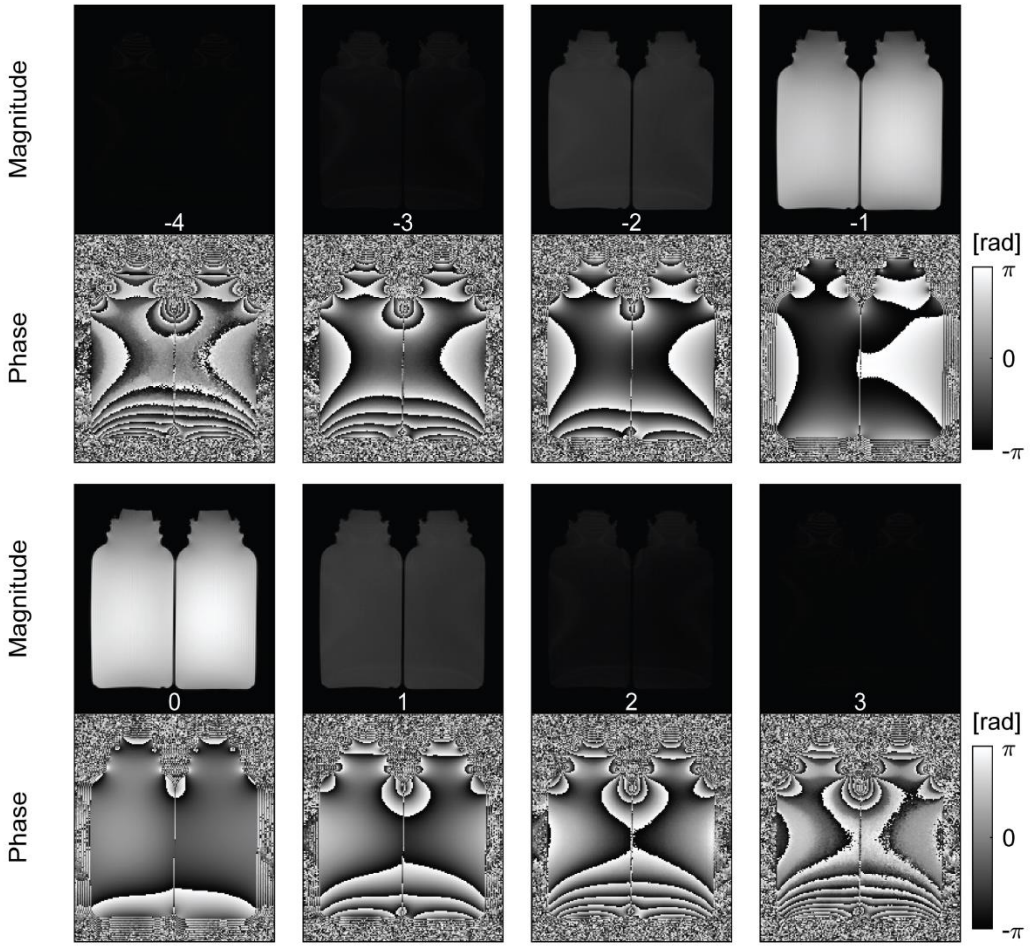

Supporting Information Figure S2 Exemplary magnitude and phase images of the configurational modes of the phantoms calculated from the set of eight phase-cycled bSSFP volume scans with different RF phase increment in S1. Note that all magnitude images are scaled equally.

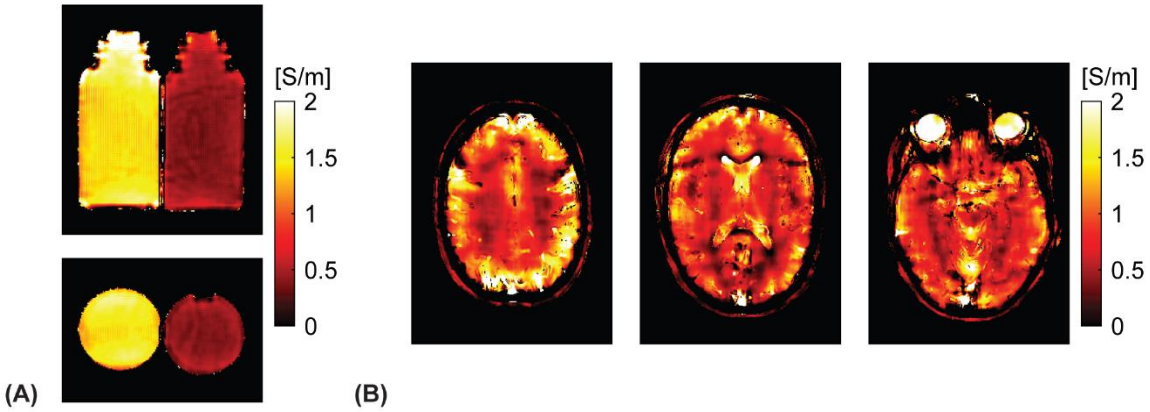

Supporting Information Figure S3 (A) Exemplary coronal and axial images of the reconstructed conductivity before applying the magnitude based boundary-preserving median filter. (B) Likewise, the reconstructed conductivity before applying the magnitude based boundary-preserving median filter for the exemplary axial slices of the in-vivo brain.